Micromechanics of intergranular creep failure under cyclic loading

van der Giessen, E.; Tvergaard, V.

Published in:
Acta Materialia

DOI:
10.1016/1359-6454(95)00399-1

Pergamon

1359-6454(95)00399-1

Acta mater. Vol. 44, No. 7, pp. 2697–2710, 1996

Published by Elsevier Science Ltd

1359-6454/96 $15.00 + 0.00

MICROMECHANICS OF INTERGRANULAR CREEP FAILURE UNDER CYCLIC LOADING

E. VAN DER GIESSEN[1] and V. TVERGAARD[2]

[1]Laboratory for Engineering Mechanics, Delft University of Technology, PO Box 5033, Delft, The Netherlands and [2]Department of Solid Mechanics, The Technical University of Denmark, Lyngby, Denmark

(Received 24 July 1995; in revised form 10 October 1995)

Abstract—This paper is concerned with a micromechanical investigation of intergranular creep failure caused by grain boundary cavitation under strain-controlled cyclic loading conditions. Numerical unit cell analyses are carried out for a planar polycrystal model in which the grain material and the grain boundaries are modelled individually. The model incorporates power-law creep of the grains, viscous grain boundary sliding between grains as well as the nucleation and growth of grain boundary cavities until they coalesce and form microcracks. Study of a limiting case with a facet-size microcrack reveals a relatively simple phenomenology under either balanced loading, slow–fast loading or balanced loading with a hold period at constant tensile stress. Next, a (non-dimensionalized) parametric study is carried out which focusses on the effect of the diffusive cavity growth rate relative to the overall creep rate, and the effects of cavity nucleation and grain boundary sliding. The model takes account of the build up of residual stresses during cycling, and it turns out that this, in general, gives rise to a rather complex phenomenology, but some cases are identified which approach the simple microcrack behaviour. The analyses provide some new understanding that helps to explain the sometimes peculiar behaviour under balanced cyclic creep. *Copyright © 1996 Acta Metallurgica Inc.*

1. INTRODUCTION

In polycrystalline metals at elevated temperatures, creep fracture under monotonic loading occurs mainly by intergranular cavitation and microcracking. Cavities nucleate and grow most rapidly on grain boundary facets normal to the maximum principal tensile stress (e.g. Refs [1, 2]), and facet microcracks form by coalescence of cavities. In studies of grain boundary cavity growth, the mechanism of creep constrained cavitation [3] plays an important role, and has been modelled in some detail by representing a cavitating facet as a penny-shaped crack by Rice [4] and Tvergaard [5]. Other axisymmetric models have been used to incorporate the important effect of grain boundary sliding [6, 7]. In addition, planar analyses of unit cells containing many grains have been carried out by Hsia *et al.* [8] to investigate the combined effect of microcracks and grain boundary sliding. Similar multi-grain models have subsequently been used by Van der Giessen and Tvergaard [9, 10] to study the interaction between neighbouring cavitating facets, and the final link up of the facet microcracks, which form by coalescence of the grain boundary cavities.

If instead the material is subjected to cyclic loading, both creep damage and fatigue are likely failure mechanisms. In a range of very slow cycling there will be sufficient time for creep and diffusion mechanisms to dominate, leading to intergranular creep fracture, whereas a typical transgranular fatigue fracture tends to develop in the opposite situation of very rapid cycling. In the whole range between these two extremes the failure process is usually termed creep–fatigue interaction. The micromechanisms of this process that predominate in different ranges of stress, temperature, loading frequency and wave-shape have been discussed by several authors (e.g. Refs [11, 12]); Riedel [13] has given a comprehensive overview.

For the range of slow cycling, where creep failure mechanisms dominate, there have been several attempts to explain why some materials show cavitation even under balanced cyclic loading with zero mean stress, e.g. see the discussion by Riedel [13]. Diffusive cavity growth follows an equation linear in stress, which should not result in cavity growth under balanced cycling. Some speculations have focussed on the need to account for nonlinearities in the diffusion equation, while others have focussed on an effect of the elastic transient during the first part of cycling. However, Riedel [13] has argued that both effects are so small that they could hardly play any role.

In the present paper we use the plane strain multi-grain cell model of Van der Giessen and Tvergaard [9, 10, 14] to study the effect of cyclic loading on a polycrystalline metal. No fatigue failure mechanisms are accounted for in these studies, so the results are only relevant to a range of relatively

slow cycling, or to an early stage of cycling, where intergranular creep failure mechanisms are completely dominant. Relating to the question of cavitation under balanced cycling, these studies have the potential of revealing some of the main mechanisms. That is, the cavity growth model accounts for the interaction of creep and diffusion, and the model also incorporates complex mechanisms such as continuous cavity nucleation, creep constrained cavitation and grain boundary sliding. With these nonlinear effects included in the model, one cannot directly see what the behaviour should be like in situations such as balanced cycling. In addition to these studies, the model is also used to consider the effect of unbalanced cycling. The contributions of some of the key mechanisms are separated out by way of a parametric study.

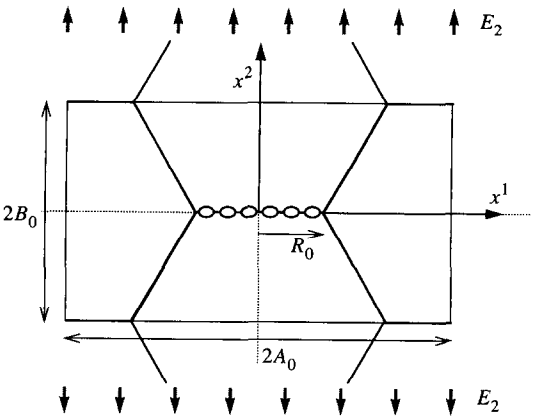

Fig. 2. Unit cell of the planar polycrystal material model, comprising two hexagonal grains. Only the shaded area is analyzed in view of symmetry.

2. FORMULATION OF THE MODEL PROBLEM

We envision the material to be subjected to typical low-cycle fatigue conditions at constant temperature. That is, the material is loaded in uniaxial tension according to a strain-controlled loading programme of the type illustrated in Fig. 1. In general, each cycle of strain between $\pm\frac{1}{2}\Delta\epsilon^C$ consists of a loading period of duration t_l during which the material is subjected to a constant tensile strain-rate, a strain hold period of duration t_h and an unloading period of t_u, during which the applied strain-rate is compressive. The total cycle duration is $t_c = t_l + t_h + t_u$. Commonly, three standard wave-shape patterns are considered: (i) balanced loading (or equal ramp cycles) where $t_l = t_u$, without a hold period ($t_h = 0$); (ii) slow–fast loading where the tensile loading is done over a longer period of time than the unloading ($t_l > t_u$, $t_h = 0$), so that strain-rate in tension is lower than in compression; (iii) tension hold, i.e. balanced loading and unloading but with a significant hold period, $t_h > 0$.

We shall study the deformation and failure mechanisms under this type of loading for a planar model of a polycrystalline material, which is built up as a regular array of regular hexagonal grains with initial facet width $2R_0$. Assuming a certain degree of periodicity in the microstructure, attention can be confined to the unit cell shown in Fig. 2 with initial dimensions $A_0 = 3R_0$ by $B_0 = \sqrt{3}R_0$. The material is supposed to be subjected to the macroscopic strain history as described above, under uniaxial stress conditions in the x^2-direction (x^i is a Cartesian coordinate system indicated in Fig. 2). That is, the overall strain E_2 of the unit cell is taken to be prescribed according to the strain history $\epsilon(t)$ in Fig. 1, while the remote transverse stress $\Sigma_1 = 0$. At all times, the central grain facet coinciding with $x^2 = 0$ is transverse to the principal stress direction.

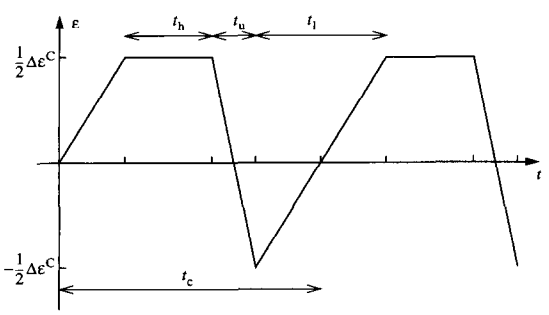

Fig. 1. Strain-controlled remote cyclic loading conditions.

The following micromechanisms, that are typical for polycrystalline metals and alloys at elevated temperatures, are being considered: (i) dislocation creep inside the grains, (ii) viscous grain boundary sliding, (iii) the nucleation and (iv) growth of cavities on the grain boundaries. The material models that we use to describe these mechanisms have been developed in a number of papers (e.g. Refs [5, 6]) and described in some detail in previous creep rupture studies [7, 9, 14]; here, we shall only give a summary for completeness. Creep deformations are taken to be characterized by the power-law relationship

$$\dot{\epsilon}_e^C = \dot{\epsilon}_0 \left(\frac{\sigma_e}{\sigma_0}\right)^n, \tag{2.1}$$

between the effective Mises stress σ_e and the corresponding creep strain-rate $\dot{\epsilon}_e^C$ with a creep exponent n. Here, $\dot{\epsilon}_0$ and σ_0 are reference strain-rate and stress quantities.

Following Ashby [15], grain boundaries are modelled as thin layers of thickness w that slide in a linear viscous manner such that the relative sliding velocity $\dot{v}$ of adjacent grains is related linearly to the shear stress τ in the grain according to

$$\tau = \eta_B \frac{\dot{v}}{w}. \tag{2.2}$$

We shall treat the viscosity η_B as a separate material parameter, which can be specified conveniently in terms of the strain-rate like parameter [16, 7]

$$\dot{\epsilon}_B = \dot{\epsilon}_0 \Big/ \left(2\sqrt{3}\,\frac{R_0}{w}\,\eta_B\,\frac{\dot{\epsilon}_0}{\sigma_0}\right)^{n/(n-1)}.$$

Comparing with the creep rate from (2.1), free grain boundary sliding is characterized by $\dot{\epsilon}_e^C/\dot{\epsilon}_B = 0$, while $\dot{\epsilon}_e^C/\dot{\epsilon}_B \to \infty$ in the limit of no sliding.

The distribution of grain boundary cavities is characterized by their radius a, their spacing b and cavity tip angle ψ, as illustrated in Fig. 3. The generation of new cavities is regarded as a nucleation process that continues with creep deformation, and is governed by the nucleation law

$$\dot{N} = \begin{cases} F_n(\sigma_n/\Sigma_0)^2\dot{\epsilon}_e^C, & \sigma_n > 0; \\ 0 & \sigma_n \leqslant 0; \end{cases} \tag{2.3}$$

in terms of the cavity density N defined per unit undeformed grain boundary area. In this expression, σ_n is the average stress normal to the grain boundary, and F_n and Σ_0 are material constants. It is assumed that cavities nucleate only under a tensile stress normal to the facet. Cavity nucleation changes the average cavity spacing b, and so do the finite strain rate effects associated with the in-plane deformations ϵ_1 and ϵ_2 in the grain boundary. Thus,

$$\frac{\dot{b}}{b} = \frac{1}{2}(\dot{\epsilon}_1 + \dot{\epsilon}_2) - \frac{1}{2}\frac{\dot{N}}{N}. \tag{2.4}$$

The cavity size a increases as the void grows, due to both grain boundary diffusion and creep of the grain material. It is assumed that the tip angle ψ maintains a constant value throughout the process. The volumetric growth rate $\dot{V}$ of a cavity is expressed as

$$\dot{V} = \dot{V}_1 + \dot{V}_2, \quad \text{for } a/L \leqslant 10,$$

$$f = \max\left[\left(\frac{a}{b}\right)^2, \left(\frac{a}{a+1.5L}\right)^2\right], \tag{2.5}$$

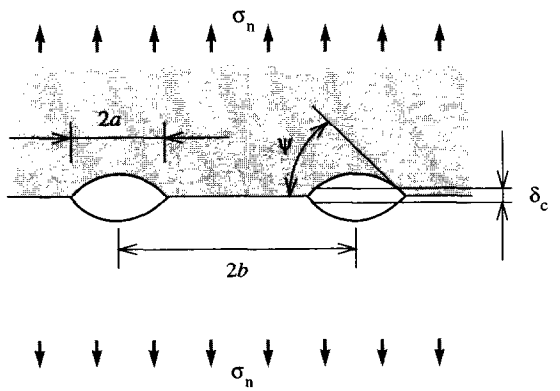

Fig. 3. Geometry of spherical-caps shaped cavities on a grain boundary subjected to a remote facet normal stress σ_n.

where

$$\dot{V}_1 = 4\pi\mathscr{D}\,\frac{\sigma_n - (1-f)\sigma_s}{\ln\left(\frac{1}{f}\right) - \frac{1}{2}(3-f)(1-f)}, \tag{2.6}$$

$$\dot{V}_2 = \begin{cases} 2\pi\dot{\epsilon}_e^C a^3 h(\psi) m\left[\alpha_n\left|\frac{\sigma_m}{\sigma_e}\right| + \beta_n(m)\right]^n, & \left|\frac{\sigma_m}{\sigma_e}\right| > 1; \\ 2\pi\dot{\epsilon}_e^C a^3 h(\psi)[\alpha_n + \beta_n(m)]^n \frac{\sigma_m}{\sigma_e}, & \left|\frac{\sigma_m}{\sigma_e}\right| \leqslant 1. \end{cases} \tag{2.7}$$

with

$$m = \operatorname{sign}\left(\frac{\sigma_m}{\sigma_e}\right),$$

and $h(\psi) = [(1+\cos\psi)^{-1} - \frac{1}{2}\cos\psi]/\sin\psi$ the cavity shape parameter. The parameter $\mathscr{D} = D_B\delta_B\Omega/kT$ in the growth rate expression (2.6) due to diffusion is the grain boundary diffusion parameter, with $D_B\delta_B$ denoting the boundary diffusivity, Ω the atomic volume, k Boltzmann's constant and T the absolute temperature. The sintering stress σ_s in equation (2.6) will be neglected, as it often is much smaller than the facet normal stress σ_n (e.g. Refs [5–10]). An important aspect for cyclic creep, however, is that cavities may shrink to very small size under a compressive facet stress, but we will assume here that the cavity nucleus still remains present. Thus, it is assumed that existing cavities do not completely disappear by sintering, and therefore need not be re-nucleated under tension. Furthermore, in the creep growth expression (2.7), σ_m and σ_e are the average mean and Mises stress, respectively, remote from the void. The constants appearing in (2.7) are given by $\alpha_n = 3/2n$ and

$$\beta_n(m) = \frac{(n-1)[n+g(m)]}{n^2};$$

$$g(1) = 0.4319, \quad g(-1) = 0.4031.$$

In previous creep rupture studies [7, 14, 9], the small difference between $\beta_n(1)$ and $\beta_n(-1)$ in the solution according to Budiansky *et al.* [17] has been irrelevant, but for cyclic creep situations where negative values of σ_m should be expected, we do account for this difference. However, we have not found any significant numerical influence in our computations. The parameter

$$L = [\mathscr{D}\sigma_e/\dot{\epsilon}_e^C]^{1/3} \tag{2.8}$$

in equation (2.5) has been introduced by Needleman and Rice [18]. It serves as a stress- and temperature-dependent length scale governing the coupling between diffusive and creep contributions to void growth by way of the selection in equation (2.5) of the value for f to be used in the diffusive growth expression (2.6). For large values of this length scale,

say $a/L < 0.1$, cavity growth is dominated by diffusion, while for larger values of a/L creep growth becomes more and more important (see Refs [18, 19]). As a consequence, cavity growth in situations where $a/L < 0.1$ or so, is likely to be constrained by creep of the material surrounding the cavitating facet, whereas this creep constraint reduces with increasing a/L (see Refs [3–5]).

With $\dot{V}$ according to equation (2.5) the growth rate of the cavity radius is obtained through $\dot{a} = \dot{V}/(4\pi a^2 h(\psi))$. Nucleation and growth of cavities give rise to a separation δ_c between the two adjacent grains (see Fig. 3). The rate of change of this separation is determined through equations (2.4) and (2.5) as

$$\dot{\delta}_c = \frac{\dot{V}}{\pi b^2} - \frac{2V}{\pi b^2}\frac{\dot{b}}{b}. \tag{2.9}$$

When the ratio a/b reaches the value 0.7 during the process, cavity coalescence is assumed to occur by failure of the ligament between cavities. Thus, a new microcrack is formed or an existing microcrack is extended. Under cyclic loading it may be possible that such a microcrack closes up again, but it is unlikely that previously coalesced cavities can heal to re-form cavities. Therefore, the microcracks are regarded to simply make contact again when the actual separation between grains has become as small as the separation δ_c at coalescence, and the microcrack can immediately open-up again when local loading becomes tensile.

3. METHOD OF ANALYSIS

The constitutive models for the mechanisms discussed in Section 2 are embedded in a finite strain formulation of the governing equations describing the material behaviour inside the unit cell of Fig. 2. The formulation uses a convected coordinate description with the x^i-coordinates as material coordinates. The metric tensors in the reference and current deformed configurations are denoted by g_{ij} and G_{ij}, respectively.

The total Lagrangian strain-rate within each grain is written as the sum of the elastic part $\dot{\eta}_{ij}^{E}$ and the creep part $\dot{\eta}_{ij}^{C}$. Thus, with the usual linear elastic stress–strain relationship $\overset{\nabla}{\tau}{}^{ij} = R^{ijkl}\dot{\eta}_{kl}^{E}$, in terms of the Young's modulus E and the Poisson's ratio ν, the constitutive relations for the elastic-creeping grain material can be written as

$$\overset{\nabla}{\tau}{}^{ij} = R^{ijkl}(\dot{\eta}_{kl} - \dot{\eta}_{kl}^{C}),$$

where $\overset{\nabla}{\tau}{}^{ij} = \dot{\tau}^{ij} + (G^{ik}\tau^{jl} + G^{jk}\tau^{il})\dot{\eta}_{kl}$, is the Jaumann stress-rate in convected coordinates. The creep part of the strain-rate accounts for isotropic power-law creep through

$$\dot{\eta}_{ij}^{C} = \dot{\epsilon}_e^{C}\frac{3}{2}\frac{s_{ij}}{\sigma_e},$$

with the effective creep-rate $\dot{\epsilon}_e^{C}$ given by equation (2.1). Here, the effective Mises stress $\sigma_e = \sqrt{\frac{3}{2}s_{ij}s^{ij}}$ and the stress deviator $s^{ij} = \tau^{ij} - \frac{1}{3}G^{ij}\tau_k^k$ are specified directly in terms of the Kirchhoff stresses τ^{ij}, thus neglecting the small, elastic volume changes.

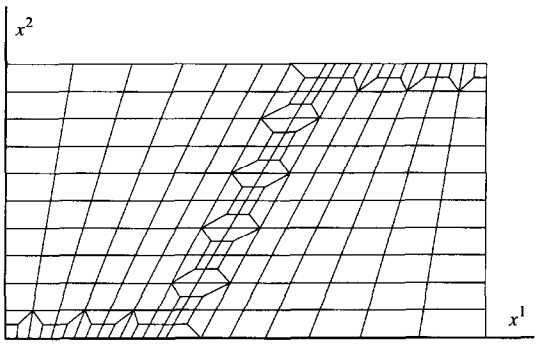

Fig. 4. Finite element mesh used for the quarter cell in Fig. 2.

The boundary conditions for the quarter cell in Fig. 2, which implement the loading programme discussed previously, and which respect the symmetry properties of the cell, are as follows. With $\dot{u}^i$ and T^i denoting the velocity components and the nominal traction components in the reference configuration, we have

$$\dot{u}^1 = 0, \quad T^2 = 0 \quad \text{along } x^1 = 0;$$

$$\dot{u}^1 = \dot{U}_1, \quad T^2 = 0 \quad \text{along } x^1 = A_0;$$

$$\dot{u}^2 = 0, \quad T^1 = 0 \quad \text{along } x^2 = 0;$$

$$\dot{u}^2 = \dot{E}_2 B, \quad T^1 = 0 \quad \text{along } x^2 = B_0.$$

The macroscopic strain-rate $\dot{E}_2$ follows immediately from the prescribed strain history $\epsilon(t)$, and the associated remote stress Σ_2 is computed from

$$\Sigma_2 = \frac{1}{A}\int_0^{A_0} T^2|_{x^2 = B_0}\,\mathrm{d}x^1.$$

Here, B and A are the current height and width of the cell. The uniform velocity $\dot{U}_1$ is determined so that the average transverse stress Σ_1,

$$\Sigma_1 = \frac{1}{B}\int_0^{B_0} T^1|_{x^1 = A_0}\,\mathrm{d}x^2,$$

maintains the constant value $\Sigma_1 = 0$.

The numerical procedure used to simulate the creep and failure process in a planar cell analysis of the present type has been outlined in some detail in Refs [7, 14], and will only be briefly recapitulated here. All grains in the polycrystal are modelled by a mesh consisting of quadrilateral finite elements, each being built up of four linear displacement triangular subelements arranged in a "crossed triangle" configuration. The mesh for the quarter unit cell that has been used for all computations here is shown in

Fig. 4. Cavitation is treated by employing a "smeared out" model in which each grain facet with its discrete distribution of cavities of radius a and half spacing b is replaced by a grain boundary layer with continuous distributions $a(x)$, $b(x)$ along the layer. The average separation between grains, $\delta_c(x)$, defines the thickness of this grain boundary layer. Special grain boundary elements are used to implement the cavitation process and the associated thickening of the boundary layer, according to equation (2.9), as well as to account for viscous grain boundary sliding, according to equation (2.2). For computational reasons, fictitious layers of linear elastic springs are added to the grain boundary layers: one with a normal stiffness k_n and one with a tangential stiffness k_s. The normal stress σ_n and shear stress τ at the grain boundary are then governed by the following constitutive equations

$$\dot{\sigma}_n = k_n(\dot{\delta} - \dot{\delta}_c), \quad \dot{\tau} = k_s(\dot{v} - \dot{v}_v),$$

with $\dot{\delta}$ and $\dot{v}$ being the actual normal thickening rate and relative sliding velocity, respectively, and with the inelastic components $\dot{\delta}_c$ and $\dot{v}_v$ being given by way of equations (2.9) and (2.2), respectively. Using large values of the stiffnesses of the fictitious elastic layers ensures that the deviations $\dot{\delta} - \dot{\delta}_c$ and $\dot{v} - \dot{v}_v$ are kept small: $k_n = k_s \approx 10E/R_0$. When cavity coalescence takes place (see Section 2), the stresses σ_n and τ, as well as the stiffnesses k_n, k_s reduce to zero. In the computations, the values are stepped down to zero in a number of incremental steps to avoid numerical instability problems. When the two faces of a microcrack come into contact during the process, the value of the normal stiffness k_n is instantaneously reset from zero to the aforementioned non-zero value, now in order solely to represent the contact condition. As we consider cavitation to take place only on the central grain facet in the cell (see Fig. 2), symmetry implies that the value of k_s on that facet is irrelevant, also upon restoring contact. This modelling of the cavitating grain boundaries is implemented in the finite element description by means of special purpose grain boundary elements (not explicitly shown in Fig. 4).

The governing equations for the grains as well as the grain boundary layers are formulated within a linear incremental framework based on an incremental version of the virtual work equation (see Refs [7, 14]). An equilibrium correction is applied to prevent drifting of the solution from the true equilibrium path. A forward gradient approach was applied both to the creep constitutive equations (2.1) (see Ref. [5]) and to the constitutive equations describing cavitation and grain boundary sliding (see Ref. [7]), to increase the stable step size.

For conciseness, all results will be presented in nondimensional form. For that purpose, all stresses in the problem may be normalized by a reference stress Σ_e^0, which will be specified presently, while all time scales are normalized by the reference time t_R defined by

$$t_R = \Sigma_e^0/(E\dot{E}_e^C),$$

with $\dot{E}_e^C$ being the creep strain rate corresponding to Σ_e^0 through the power law (2.1). With these parameters, the applied strain range $\Delta\epsilon^C$ can be normalized as $\Delta\epsilon^C/(\dot{E}_e^C t_R)$, or equivalently, $\Delta\epsilon^C/(\Sigma_e^0/E)$. Now, we define Σ_e^0 in such a way that $\dot{E}_e^C$ is identical to the minimum applied strain rate in either tension or compression (see Fig. 1), i.e.

$$\dot{E}_e^C = \min[|\Delta\epsilon^C/t_l, \Delta\epsilon^C/t_u|],$$

and

$$\Sigma_e^0 = \sigma_0(\dot{E}_e^C/\dot{\epsilon}_0)^{1/n}.$$

With this, it follows that

$$\frac{\Delta\epsilon^C}{\dot{E}_e^C t_R} = \max\left[\frac{t_l}{t_R}, \frac{t_u}{t_R}\right],$$

implying that $\Delta\epsilon^C/(\dot{E}_e^C t_R)$ is no longer an independent parameter once the reference time scale t_R has been chosen. Careful examination of the governing equations, including boundary and initial conditions, then reveals that the entire process of cyclic creep studied here as a function of t/t_R is determined by the following nondimensional group

$$\left(\frac{t_l}{t_R}, \frac{t_h}{t_R}, \frac{t_u}{t_R}; \frac{\Sigma_e^0}{E}, \left(\frac{a}{L}\right)_I, \left(\frac{a}{b}\right)_I, \right.$$

$$\left. \frac{b_I}{R_0}, n, \nu, h(\psi), \frac{F_n}{N_I}, \frac{\dot{\epsilon}_B}{\dot{E}_e^C}\right). \quad (3.1)$$

Here, the subscript I indicates the initial value of the pertinent quantity, and $N_I = 1/(\pi b_I^2)$. Furthermore, L_I is the value of L corresponding to using the reference effective stress Σ_e^0 and creep strain rate $\dot{E}_e^C$ in equation (2.8). The normalization factor Σ_0 in the nucleation law (2.3) is identified with the reference effective stress Σ_e^0. It should be noted that equation (3.1) comprises the minimal set of governing parameters, but also that it does have the drawback that the influence of, for instance, the strain range $\Delta\epsilon^C$ and the loading frequency t_c is incorporated in a rather intricate manner. For example, increasing the tensile period t_l and keeping all other physical parameters unchanged, will consecutively affect $\dot{E}_e^C$, Σ_e^0, t_R and L_I. The same is true when only the strain range $\Delta\epsilon^C$ is changed since this changes the applied strain-rate $\dot{E}_e^C$.

4. CYCLIC BEHAVIOUR OF MICROCRACKS

In modelling intergranular creep rupture the behaviour of a microcrack in a creeping solid has played an important role since Rice [4] suggested modelling a cavitating grain boundary facet as a penny-shaped crack. Using this model it was shown

[4] that a cavitating grain boundary facet behaves as an open microcrack when the rate of dislocation creep of the grain is too slow to accommodate rapid diffusive cavity growth, even in cases where the area fraction of cavities on the facet is quite low. To model material behaviour in this creep constrained range, Hutchinson [20] developed an expression for the rate of creep of a microcracked solid, and Tvergaard [5] used the penny-shaped crack model to further study the range of transition between creep constrained behaviour and unconstrained cavity growth.

Also for cyclic loading it is likely that the behaviour of an open microcrack normal to the maximum principal tensile stress can serve as an important reference case to obtain insight in the material behaviour. This should be relevant in cases where the creep rate during cycling is so low that creep constrained cavitation would be active throughout the cycle.

Therefore, we first consider a penny-shaped microcrack in a material subject to balanced cycling ($t_h = 0$, $t_l = t_u$). If the crack is initially closed, it will open up during the first tensile half cycle ($0 < t < \frac{1}{2}t_l$), but it will be completely closed again approximately half-way during the subsequent compressive half cycle ($\frac{1}{2}t_l < t < \frac{3}{2}t_l$), when the applied strain E_2 is back to zero ($t = t_l$). During the second half of the compressive wave ($t_l < t < \frac{3}{2}t_l$), a contact pressure will build up on the crack surface. This will give a non-symmetry of the cycle that will tend to wedge the crack further open in subsequent cycles ($t > \frac{3}{2}t_l$). Thus, for balanced cycling with a constant amplitude of strain it is directly understandable that the crack will end up cycling between an open state and a state where the crack just reaches complete closure at the moment where the next tensile half cycle starts. This will be called in what follows: "the simple microcrack model".

This simple picture will be further investigated here by numerical plane strain simulations for the unit cell model discussed in Section 2, taking the central facet in Fig. 2 to be an open crack ($\sigma_n = 0$ when no contact), either with or without grain boundary sliding on the other facets. Here, as well as in the subsequent section, the grain material is taken to be specified by $\nu = 0.3$ and $n = 5$. The strain range during cycling is specified through $\Sigma_e^0/E = 0.5 \times 10^{-3}$.

With freely sliding grain boundaries, under balanced loading specified by $t_l = t_u = 30t_R$, the time variation of the crack opening δ is shown in Fig. 5(a). Here, the crack opening is normalized by its initial half-width R_0 and the remote strain range $\Delta\epsilon^C$. The microcrack opening shown here is actually measured at the centre of the facet, but Fig. 5(b) shows that the opening is practically constant all over the facet, throughout the cycling. The figures also show that the behaviour of the two-grain model with free sliding agrees with the expectations for the simple penny-shaped crack model. In fact, crack surface contact is

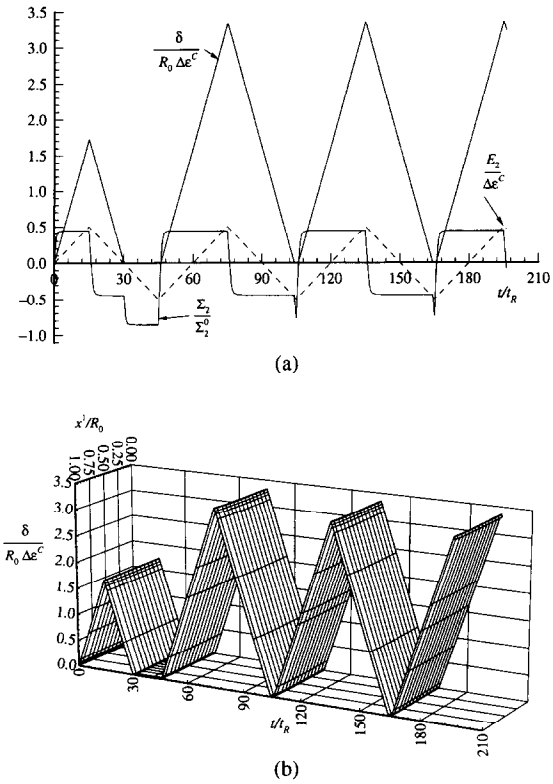

Fig. 5. Normalized microcrack opening evolution in a microcracked material with freely sliding grain boundaries under balanced loading: (a) the opening δ at the centre $x^1 = x^2 = 0$ (see Fig. 2) of the microcrack (E_2 is the prescribed macroscopic strain, Σ_2 is the macroscopic stress response); (b) the opening distribution $\delta(x^1)$ along the half facet $0 \leqslant x^1 \leqslant R_0$.

regained during a period of the first cycle, which results in twice the maximum crack opening during the second cycle, and subsequently the maximum crack opening is the same in each cycle while crack closure is only reached briefly.

Figure 5(a) also shows the macroscopic stress response, normalized by the reference stress Σ_2^0 corresponding to steady-state creep of the undamaged material [i.e. $\Sigma_2^0 = \Sigma_e^0/(\frac{1}{2}\sqrt{3})$]. It is seen that the frequency of loading is low enough for the chosen parameters that steady-state creep is attained during each wave. Closure of the crack at $t/t_R = 30$ is observed to suddenly raise the stress from the value for the microcracked material, $|\Sigma_2/\Sigma_2^0| \simeq 0.5$, to that for the undamaged material, $|\Sigma_2/\Sigma_2^0 \simeq 0.87$. The latter figure being smaller than unity is explained from the fact that even in the undamaged material there is grain boundary sliding. The overall effect of grain boundary sliding is that the creep rate according to equation (2.1) is increased by a factor $(f^*)^n$, with f^* being the so-called stress enhancement factor (see e.g. Refs [1, 13, 14, 16]). Hence, it is easily shown that we can write $|\Sigma_2/\Sigma_2^0| = (f^*)^{-n/(n+1)}$, and using the value $f^* = 1.19$ for the present value of $n = 5$ (from Refs

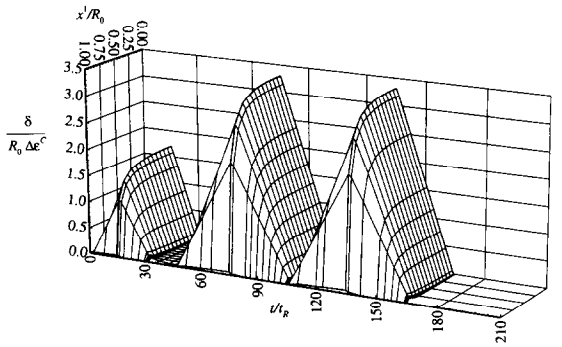

Fig. 6. Evolution of the microcrack opening distribution $\delta(x^1)$ along the half facet $0 \leqslant x^1 \leqslant R_0$ in a microcracked material without grain boundary sliding under balanced loading.

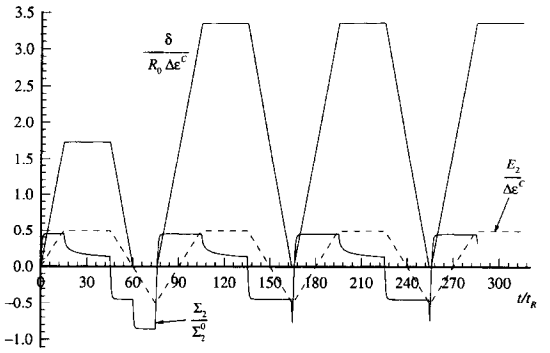

Fig. 8. Evolution of the normalized microcrack opening at the centre of the microcrack in a material with freely sliding grain boundaries under cyclic loading with a hold period $t_h = t_u = t_l$.

[14, 16]) we accurately recover the observed ratio in Fig. 5.

The same model problem has been reanalysed with a very high grain boundary viscosity [$\log(\dot{E}_c^C/\dot{\epsilon}_B) = 3.5$], so that grain boundary sliding is essentially suppressed (cf. Refs [9, 14]). As illustrated in Fig. 6, this gives qualitatively the same behaviour as found above in the case of free sliding. In the central part of the facet the behaviour is also quantitatively nearly the same, whereas the crack opening decays towards zero as the facet edge is approached. This case is the plane strain analogue of the penny-shaped crack case discussed above, although it is seen in Fig. 6 that the viscosity has not been chosen large enough to completely suppress the crack opening at the facet edge.

The analysis of Fig. 5, with free grain boundary sliding, has been repeated for two different kinds of non-symmetric loading. Figure 7 shows the result of slow–fast loading by taking $t_u = \frac{1}{2}t_l$, where the longer tension period would tend to give more creep in tension. This type of effect should be even more pronounced in the case of Fig. 8, where a hold period in tension has been added in each cycle, i.e. $t_h = t_l = t_u$. In both cases it is seen that the behaviour remains very similar to that found in Fig. 5(a) for

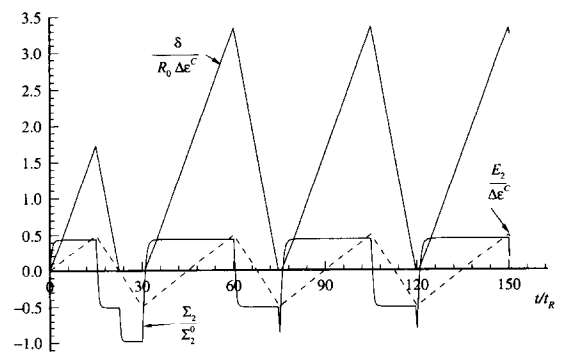

Fig. 7. Evolution of the normalized microcrack opening at the centre of the microcrack in a material with freely sliding grain boundaries under slow–fast loading with $t_u = \frac{1}{2}t_l$.

balanced cycling. Thus, microcrack closure occurs after the first cycle, and the maximum microcrack opening is about twice as large in all subsequent cycles, while crack closure occurs briefly in each cycle. It is noted that with the overall strain E_2 prescribed, the hold period allows for a substantial relaxation of the stresses in the material. This is reflected in a substantial reduction of the macroscopic stress Σ_2 (see Fig. 8), while the microcrack opening remains virtually constant. Therefore, the fact that the microcrack reaches closure in each cycle is not surprising, even under the unsymmetric cycling, but if the overall stress Σ_2 were prescribed, rather than E_2, the behaviour would be different. Then, under cyclic Σ_2 loading with a time variation analogous to that shown in Fig. 1, creep in the stress hold period would give additional crack opening, and it is expected that the hold period would result in an increase of the minimum crack opening for each cycle.

5. CYCLIC CREEP CAVITATION

In this section we shall explore the development of cavitation damage under cyclic loading conditions through a parametric study of some of the key parameters in equation (3.1). All cases to be presented have used $\nu = 0.3$, a creep exponent $n = 5$ and a cavity tip angle $\psi = 75°$. The initial state of cavitation is taken to have a relatively low initial density of small cavities specified by $b_I/R_0 = 1$ and $(a/b)_I = 0.01$. Then, the main effects that are studied here are the ratio between creep and diffusive growth of cavities, through $(a/L)_I$, grain boundary sliding, the presence or absence of continuous nucleation specified by F_n, and the frequency of loading.

We start out by first considering cases where there is no cavity nucleation ($F_n = 0$) under balanced cyclic loading specified by $t_l = t_u = 30t_R$ as in the previous section. Figure 9 shows the evolution of cavitation damage in terms of a/b along the central cavitating facet during the first 15 cycles for a range of values of $(a/L)_I$ and with free grain boundary sliding. Let us

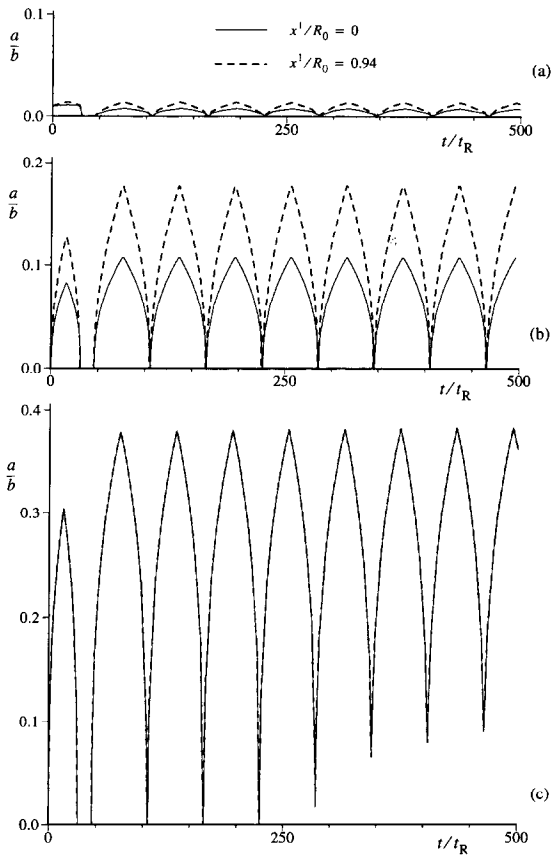

Fig. 9. Damage evolution at two points on the central facet ($x^1/R_0 = 0$ and 0.94, respectively) under balanced cyclic loading without cavity nucleation ($F_n = 0$) and with free grain boundary sliding for different values of $(a/L)_I$: (a) $(a/L)_I = 0.33$, (b) $(a/L)_I = 0.025$, (c) $(a/L)_I = 0.005$.

first look at the case where $(a/L)_I = 0.33$ so that cavity growth is dominated by creep (cf. Ref. [5]), as shown in Fig. 9(a). Cavitation develops virtually uniformly over the facet during the first cycle, while cavity growth is somewhat faster near the triple grain junction in subsequent cycles. Clearly, this must be attributed to free sliding, which gives rise to locally enhanced mean and effective stresses near the triple point. During the second tensile wave, the cavities will open up again, without having to nucleate first. Subsequent cavity growth during each tensile wave is essentially creep strain controlled, and the increase in damage is completely recovered during the compressive waves. This explains why, right from the beginning of the process, the damage steadily oscillates in time around the initial damage level.

A slightly different picture is observed in Fig. 9(b) when $(a/L)_I = 0.025$ while all other parameters have been kept unchanged. In this case, the diffusive contribution to cavity growth dominates over creep growth. Growth of the cavities is now driven primarily by the local facet normal stress, which again is considerably larger near the triple point than the average value due to sliding along the adjacent grain boundary. Therefore, already during the first tensile wave, cavity growth is quite nonuniform over the facet, but during the subsequent compressive wave, the cavities near the triple point are seen to close faster than in the centre. Hence, all cavities have essentially closed up shortly after the first half wave is complete. Contrary to the case in Fig. 9(a), the cavities grow substantially further during the second tensile wave than in the first tensile wave. This is a consequence of the fact that the time for the diffusive process for growth is twice as large as in the first tension period, but, in the subsequent compression period, it is observed that the cavities fully close again. This process continues for the next 10 or so cycles.

In the case of Fig. 9(b), creep of the grains is apparently fast enough to accommodate the more rapid cavitation near the triple point. When diffusion would be still much faster, variations of cavitation along the facet would no longer be possible. This is demonstrated in Fig. 9(c) where $(a/L)_I$ is reduced down to 0.005. As a consequence, cavity growth is constrained by the creep deformations of the surrounding grains, and the facet normal stresses σ_n along the facet are much lower in absolute value than the applied stress, which is roughly equal to Σ_2^0. This is illustrated in Fig. 10, where it is observed that during each tensile wave the normal stress rather quickly falls while the cavities expand.

Thus, at first glance, the case of very fast diffusion considered in Fig. 9(c) seems to be consistent with the simple microcrack picture discussed in the previous section: cavitation oscillates between zero and a constant maximum value corresponding to the average opening of the microcrack. However, the time-average normal stress over each tensile or compressive wave is not zero as in the case of a completely microcracked facet. After about five cycles this then leads to the situation that the cavities are no longer completely closed during compression and the minimum damage level slowly increases with

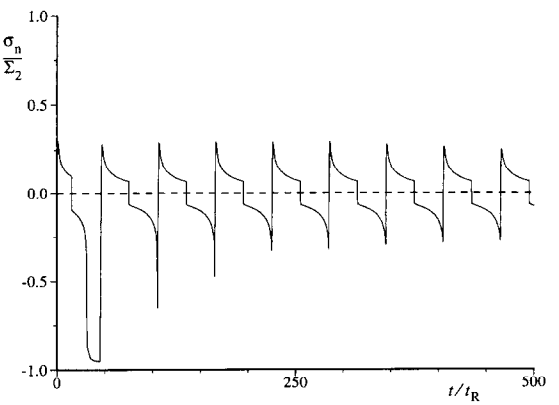

Fig. 10. Evolution of the facet normal stress σ_n in the centre of the facet during the cyclic loading case with $(a/L)_I = 0.005$ as shown in Fig. 9(c).

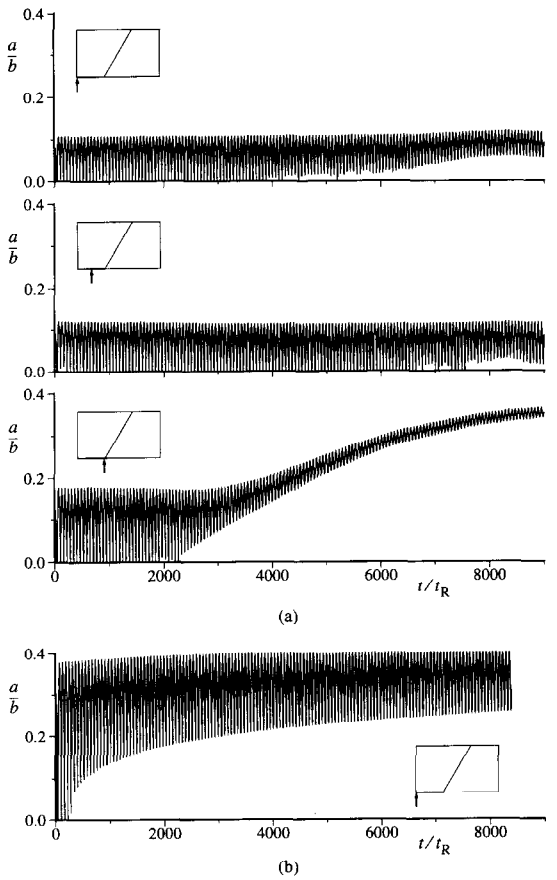

Fig. 11. Damage evolution during balanced cyclic loading without cavity nucleation ($F_n = 0$) and with free grain boundary sliding for (a) $(a/L)_I = 0.025$ [cf. Fig. 9(b)], (b) $(a/L)_I = 0.005$ [cf. Fig. 9(c)]. The inserts show the pertinent locations along the grain facet.

ongoing cycling. To see how this further evolves, we present the damage evolution over many more cycles, both for $(a/L)_I = 0.005$ in Fig. 11(b) and for $(a/L)_I = 0.025$ in Fig. 11(a). It is seen that for $(a/L)_I = 0.005$ a steady-state situation is gradually approached where the damage oscillates between a maximum value of $a/b \approx 0.4$ and a minimum value $a/b \approx 0.25$. A more complex damage accumulation behaviour is observed for the case with $(a/L)_I = 0.025$, as shown for three locations ($x^1/R_0 = 0$, 0.45 and 0.95, respectively) along the grain boundary in Fig. 11(a). The steady cycling of damage near the triple point breaks down after around 40 cycles. The minimum damage level, and subsequently also the maximum damage level, gradually increase. After around 150 cycles ($t/t_R \approx 9000$), a new steady damage oscillation seems to be approached at the triple point, also with a maximum value of $a/b \cong 0.4$, but with a narrow damage range. Elsewhere along the facet, the damage is more or less uniform and oscillates steadily between 0 and $a/b \approx 0.12$ for about the first 100 cycles. This localized damage accumulation near the triple point signifies a sort of cyclic "wedging open" of the central facet. After substantial wedging has taken place, say for more than 100 cycles, the grain deformations were very large, and we stopped the computation.

It has been mentioned above that the deviation in the behaviour presented in Fig. 11 from what one would expect on the basis of the simple microcrack picture, is due to the presence of a time-average normal facet stress. It is well-known (e.g. Refs [3, 13, 5, 7]) that under constant stress creep conditions, the normal stress on cavitating facets drops to very low values during the damage process as a consequence of creep constrained cavitation associated with these low values of $(a/L)_I$. However, under the cyclic creep conditions considered here, even for $(a/L)_I = 0.005$ there seems to be insufficient time for the facet stresses to fully relax (see Fig. 10). To get some insight into the influence of the loading frequency, we have repeated the cases of Fig. 11 under slower conditions, $t_l = t_u = 60t_R$, but with all other parameters left unchanged. By comparing the results in Fig. 12 with the corresponding ones in Fig. 11 it is seen that, qualitatively, the time-average damage evolution as a function of normalized time

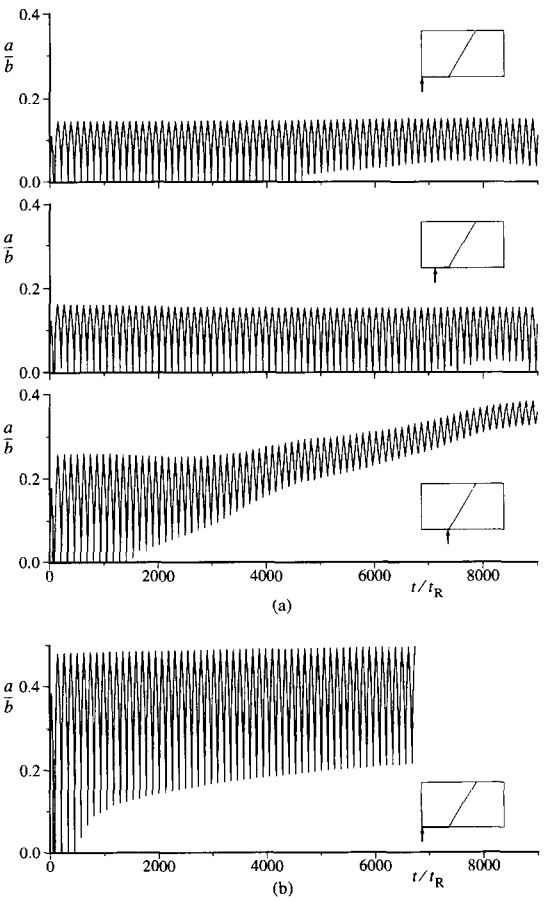

Fig. 12. Damage evolution for the same material as in Fig. 11 but at half the frequency of the cyclic loading: (a) $(a/L)_I = 0.025$, (b) $(a/L)_I = 0.005$.

appears to be independent of the loading frequency for both values of $(a/L)_I$. The time for cavitation damage to develop under tension in each cycle is now twice as long as in Fig. 11, but the maximum values of a/b are only about 50% larger. This is due to the fact that there is more time for stress redistributions associated with creep constraints.

We have seen that, especially for the case with $(a/L)_I = 0.025$, the behaviour is determined to a large extent by the fact that sliding is completely stress free. To further investigate the effects of sliding, Fig. 13 therefore gives the results for the same case but with grain boundary sliding suppressed. It is seen that the damage process evolves virtually uniformly along the facet (except during the first 20 or so cycles, when cavity closure is not complete in the immediate vicinity of the triple point; this is attributed to the numerical inaccuracies in enforcing the no-sliding condition, as also observed in Fig. 6). Furthermore, damage oscillates steadily between a maximum value ($a/b \approx 0.12$) and zero, which again is consistent with the simple microcrack picture.

The foregoing analyses are for materials that do not show any nucleation of new cavities beyond the initial damage. Such behaviour can be caused, for instance, by previous creep loading. Many materials, however, exhibit continuous cavity nucleation, not only during constant stress/load creep but also during cyclic creep (cf. Ref. [13]). Therefore, we have repeated the cases for $(a/L)_I = 0.025$ with continuous cavity nucleation being taken into account. The nucleation activity is specified through the same value $F_n = 100N_I$ in equation (2.3) as used in previous studies [9, 14]. Figure 14 shows the damage accumulation process for the free sliding case at the same three locations as in Fig. 11(a). As expected, in the beginning of the process, the average damage level increases with time due to the continuous generation of new cavities during the tension periods, which remain present under compression. Obviously, this initial average damage growth is faster near the

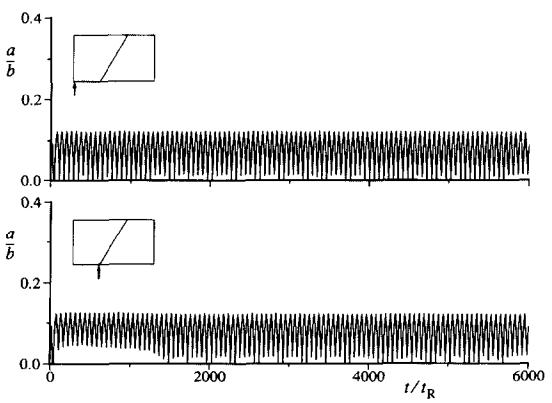

Fig. 13. Damage evolution during balanced cyclic loading without cavity nucleation ($F_n = 0$) for $(a/L)_I = 0.025$ and without grain boundary sliding.

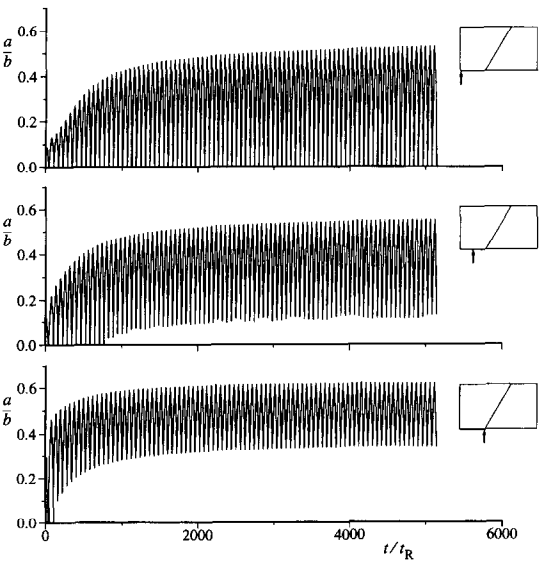

Fig. 14. Damage evolution during balanced cyclic loading for $(a/L)_I = 0.025$ and $F_n = 100N_I$ with free grain boundary sliding.

triple point due to free sliding on the adjacent grain facet. In order that this can be accommodated, a redistribution of the average internal stress field develops that constrains growth, so that a steady oscillation of damage develops. As a consequence, a substantial internal stress field builds up near the centre of the facet, which tends to completely close all cavities during the compressive waves, even though the cavity density steadily increases. We also find that the cavity density saturates as the local stress and creep rate evolve in such a way that they no longer trigger cavity nucleation according to equation (2.3). If there is no grain boundary sliding, damage accumulates faster in the central part of the facet as shown in Fig. 15. After an initial transient period, a situation develops where damage is almost uniform and is oscillating around an average value of a/b within a rather narrow range, such that even during the compression waves there is a significant amount of cavitation damage. Then, the average damage level increases rather slowly, which is again due to constraints on the cavitation process.

In the case of Fig. 15, we now also see how the slow growth of average damage actually leads to cavity coalescence (at $a/b = 0.7$), first at the centre of the facet, and then gradually propagating along the facet. At the instant of coalescence, a microcrack results with an opening corresponding to δ_c. During a subsequent comparison wave, the microcrack opening will reduce, but it is found that microcrack closure does not actually take place. This is demonstrated through the evolution of the facet normal stress at the centre of the facet plotted in Fig. 16(a): after cavity coalescence around $t/t_R \approx 4000$, the normal stress remains zero. The irreversibility of the microcrack opening is made possible by a time-average overall

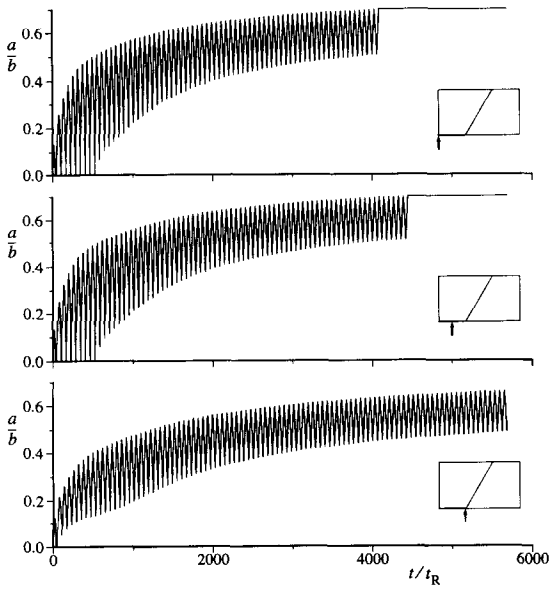

Fig. 15. Damage evolution during balanced cyclic loading for $(a/L)_I = 0.025$ and $F_n = 100N_I$ without grain boundary sliding.

dilatation which, in this plane strain model, is seen through a time-average build up of transverse strain E_1, as demonstrated in Fig. 16(b). Figure 16(a) also shows the gradual reduction of the normal stresses

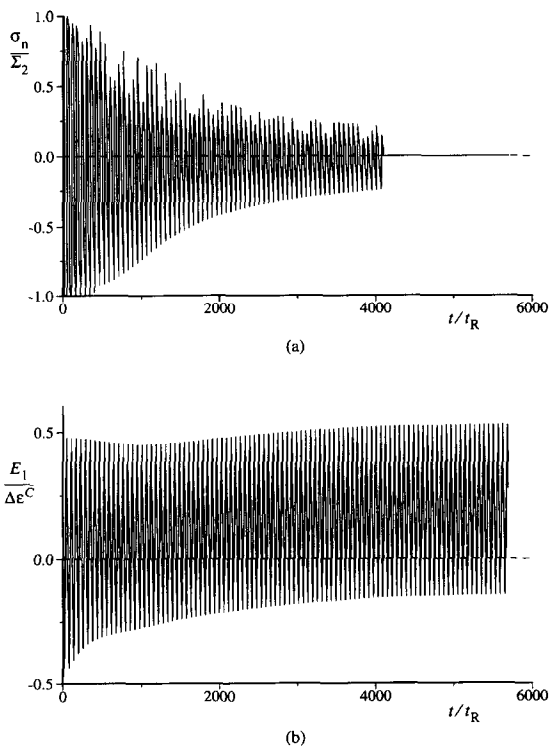

Fig. 16. Evolution of the facet normal stress σ_n in the centre of the facet (a) and the overall transverse strain E_1 evolution (b) corresponding to the case shown in Fig. 15.

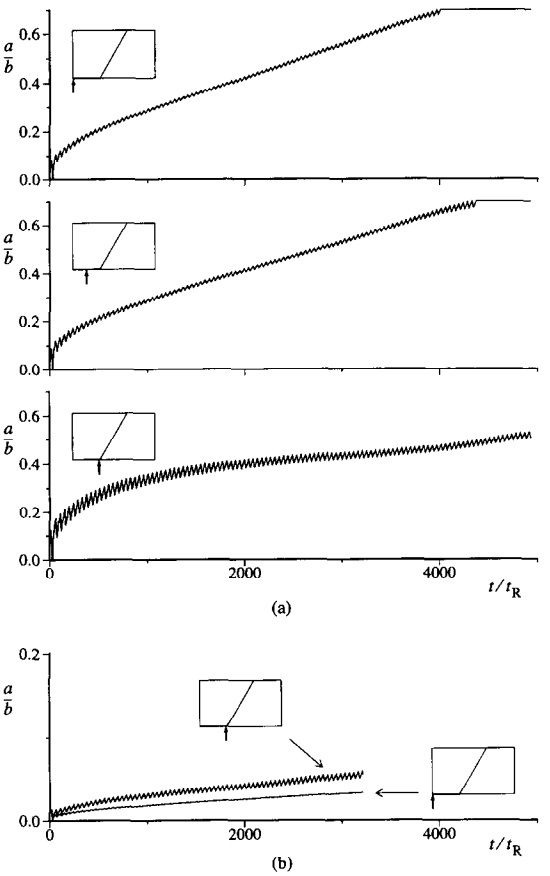

Fig. 17. Damage evolution during slow–fast loading with $t_u = \frac{1}{2}t_l$ in a material without cavity nucleation ($F_n = 0$) and with free grain boundary sliding for (a) $(a/L)_I = 0.33$, (b) $(a/L)_I = 0.025$.

during the process (especially during tension), which is associated with the constrained cavitation.

For the balanced cyclic loading situations without a hold period ($t_h = 0$) which we have considered so far, the time period in which cavitation takes place under tension is just as long as the time period available to partially reverse the previous cavitation. In contrast, during slow–fast loading with t_u smaller (or many times smaller) than t_l, there is a net time span where cavitation can develop under tension. In the limit of $t_u \to 0$, we arrive at a constant strain-rate creep test situation (as long as $t < t_l$), which is related to some extent to creep under constant stress. Creep rupture studies under constant stress conditions with a similar polycrystal model as used here have been carried out already in Refs [7, 9, 10]. As a supplement to these two types of investigations, we therefore proceed with briefly studying the influence of an intermediate slow–fast loading program specified by $t_u = \frac{1}{2}t_l$ just like in the microcrack problem of Fig. 7. Figure 17 shows the results for $(a/L)_I = 0.33$ and 0.025, in both cases assuming free sliding and no cavity nucleation; the corresponding results under balanced loading have been presented in Figs 9(a)

and (b) and 11(a). It is seen that for the creep dominated cavitation case in Fig. 17(a), the value of a/b barely shows any oscillations but rather increases "monotonically" with time, except for the immediate vicinity of the triple point. This is to a certain extent true also for the case with $(a/L)_I = 0.025$. The time available during the compressive waves is too short for the diffusive processes to eliminate the cavity growth that has taken place during the tensile waves [cf. with Fig. 11(a)]. Quite interestingly, the cavity shrinkage processes near the triple point are seen to be more efficient than elsewhere on the facet, so that the time-average damage level increases more rapidly in the centre than at the triple point. Hence, in spite of grain boundary sliding, cavity coalescence starts from the centre of the facet in this case. Finally, we have repeated the analysis for $(a/L)_I = 0.025$ of Fig. 17(b) but with cavity nucleation again being specified by $F_n = 100N_I$. Figure 18 shows that the nucleation of new cavities during the tensile waves now leads to the most rapid damage accumulation near the triple point. Due to the combination of continuous nucleation and unbalanced loading, microcracking already starts after about 20 cycles, whereas under balanced cyclic loading (cf. Fig. 14), the same model material sustained at least 10 times more cycles.

It is emphasized that the type of unbalanced cyclic loading considered here is special in that cycling occurs between fixed overall creep strain amplitudes $+\frac{1}{2}\Delta\epsilon^C$ and $-\frac{1}{2}\Delta\epsilon^C$, respectively. Such conditions can be prescribed in cyclic tests and are also relevant in some structural components, but it should be noted that cyclic creep under stress control, as often occurs in structural components, results in a different type of behaviour for unbalanced loading. Then, with a hold period in tension, the overall creep strain will increase in each cycle, and a ratchetting behaviour will be observed.

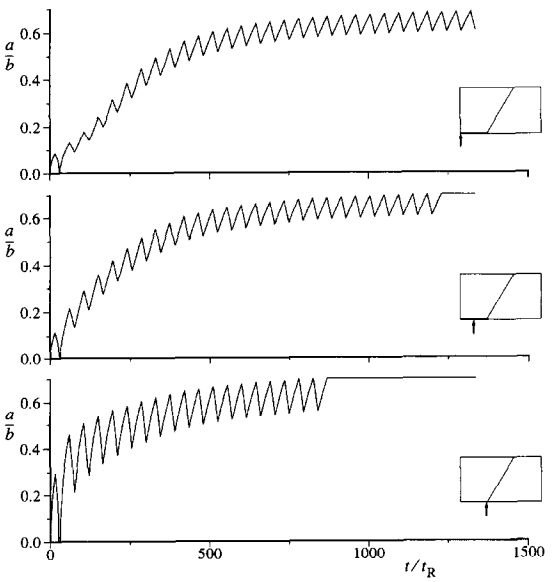

Fig. 18. Damage evolution during slow–fast loading with $t_u = \frac{1}{2}t_l$ in a material with free grain boundary sliding, for $(a/L)_I = 0.025$ and $F_n = 100N_I$.

6. DISCUSSION

The present analyses of grain boundary cavitation under cyclic loading have shown that the interaction of the different deformation and cavitation mechanisms gives rise to a complex phenomenology which would not be easily predicted *a priori*. Even for cases of balanced cyclic loading, where a number of authors have attempted to explain the expected behaviour (see, e.g. Ref. [13]), the present results show rather different behaviour for different ranges of parameter values. The major mechanisms interacting here are the nonlinear creep of grains, viscous grain boundary sliding, the possibility of creep constrained cavitation due to rapid grain boundary diffusion, and furthermore the possibility that the degree of creep constraint varies as the cavity volumes grow or decay during the cycles.

Rather important understanding of some features of the cyclic creep damage behaviour is obtained by considering what is here called "the simple microcrack model" discussed in Section 3. This is relevant because grain boundary cavitation often occurs in the creep constrained range, where a cavitating grain boundary facet behaves more or less as an open microcrack (see Ref. [4]). The present studies of open microcracks in a creeping solid under balanced cyclic loading show clearly the importance of the nonlinearity introduced by the shift between contact or loss of contact of the crack surfaces. After a transient time period, the stress and strain fields are redistributed so that contact only occurs briefly at the very end of the compressive part of the cycle. This means that during cycling the average crack opening is positive, and the crack opening cycles between twice the average opening and zero opening.

For grain boundary cavitation under balanced cyclic loading, the present analyses show some of the features expected based on this simple microcrack model. Thus, after a few cycles the cavity volume varies between zero and a more or less constant maximum value, so that the vanishing cavity volume occurs only briefly at the end of the compressive part of the cycle. However, deviations from this simple behaviour develop after a certain amount of cycling in cases of free grain boundary sliding, as is shown for different cases in Figs 9, 11 and 12. For a case with no grain boundary sliding, Fig. 13 shows rather good agreement with expectations based on the simple microcrack model. It appears that there must be an interaction between stresses induced by sliding and stresses induced by the nonlinear variation of normal stresses on the cavitating facet during cyclic changes of the cavity volumes. Clearly (Figs 10 and 12), the

strongest deviations occur near the triple grain junctions, where the cavities grow much larger than expected based on the simple model, so that cavity coalescence may result in wedge crack formation even under balanced cyclic loading. Of course, the likelihood of cavity coalescence depends on the parameter values considered. Even in a case that now agrees well with the microcrack model, such as Fig. 13, cavity coalescence will occur at the end of a tensile wave if, for instance, the value of b_1/R_0 is sufficiently reduced, for fixed values of all other parameters.

The results referred to so far emphasize that the actual behaviour is determined by the mutual ratios between the different time scales associated with the various mechanisms, as captured in the non-dimensional parameters $(a/L)_1$, t_1/t_R, t_h/t_R, t_u/t_R in equation (3.1). The role of the ratio between creep rate and diffusion rate in terms of $(a/L)_1$ under constant stress creep conditions has been made clear through many studies (see, e.g. Refs [4–6]). Creep dominated cavity growth corresponds to sufficiently large $(a/L)_1$ (>0.2, say); cavitation is diffusion dominated and constrained by creep for sufficiently small $(a/L)_1$ (<0.05, say). Under cyclic loading conditions, this simple picture no longer holds due to the interplay with the loading time scales. An important observation that arises from the results (Figs 9 and 10) is that a sufficiently long, net tensile loading time needs to be available for the creep constraint to become active. In case of insufficient time, cavity growth may be diffusion dominated at values as small as $(a/L)_1 \approx 0.05$, but growth is not creep constrained. Therefore, creep constrained diffusive growth under cyclic loading will occur only when $(a/L)_1$ is sufficiently small *and* t_1/t_R is sufficiently large. With increasingly smaller values of $(a/L)_1$ (and constant t_1/t_R), the creep constraint becomes stronger and therefore should be a limiting case where the constraints are so strong that the average facet normal stress is essentially zero, so that the simple microcrack explanation should apply exactly.

One of the striking experimental observations concerning cyclic creep failure is that some materials (copper, for example, [11]) cavitate readily under balanced cyclic loading, even though the time-averaged applied stress is zero, while others show no damage accumulation at all. As is discussed in some detail by Riedel [13], a number of explanations have been suggested in the literature, such as the irreversibility of cavity growth that takes place due to creep deformations, and elastic transient effects after reversal of loading. Our computations do not seem to support any of these suggestions. Another explanation raised in Ref. [13] is that on a microscopic scale, certain portions of the material experience a time-averaged tensile stress while other portions do not, even under applied balanced loading. This seems to be consistent with our findings in Figs 9–12 for cases that are characterized by rather small values of $(a/L)_1$.

Another obvious explanation for damage accumulation during balanced cyclic loading lies in the presence of continuous nucleation of new cavities. Then, the value of b_1/R_0 is reduced as time progresses, and thus the likelihood of cavity coalescence is increased. In Fig. 14 with free grain boundary sliding, the peak values of a/b do not quite reach the coalescence limit, but Fig. 15 illustrates a case where coalescence does lead to progressive microcrack formation after a certain amount of cavity nucleation.

It seems pertinent to emphasize the fact that the present study is concerned with strain-controlled cyclic loading, since this appears to be most relevant for many experimental cyclic creep experiments as reported in e.g. Refs [11, 13]. Depending on stress range and material parameters, balanced stress-controlled loading may give a somewhat different picture in general. However, our results in, for instance, Figs 5 and 10 show that the overall stress is very close to being balanced after an initial transient period.

Great care needs to be taken in the present type of simulations in order to accurately capture the complex phenomenology. In simulating the entire history of the process, many increments are needed to obtain sufficiently accurate results; for instance, the computation shown in Fig. 11(b) took 300,000 increments. It is therefore not feasible to prolong the computations for, e.g. balanced loading, until practical situations with number of cycles of the order of 10^3 before steady-state behaviour is attained. Nevertheless, some of the cases presented here, such as in Figs 11(b), 12(b), 13 and 14, have come close to a steady state in terms of the average damage growth rate.

In the present investigation for slow cycling the focus is on a detailed description of the interaction of the mechanisms controlling intergranular creep damage development during cyclic loading, whereas the effect of fatigue damage is not accounted for. However, creep–fatigue interaction may play a role even at slow cycling, where fatigue failure in the ligaments between grain boundary cavities may accelerate the occurrence of coalescence and thus final failure. An attempt to study this interaction has been carried out by Nielsen and Tvergaard [21], based on a simplified representation of creep cavitation. A micromechanical study of creep–fatigue interaction, taking full account of mechanisms such as grain boundary sliding, creep constrained cavitation, and the interaction between neighbouring cavitating grain boundary facets, is not yet available.

Also, it should be noted that the simple isotropic power-law creep (2.1) incorporated here, is merely a good description of steady-state creep inside the grains. Any primary creep is not accounted for. Under constant stress creep conditions, primary creep is usually of no significance for the final time to

failure; but, under the present cyclic loading conditions, primary creep or recovery is likely to be more important. However, we have not made any attempt so far to include this.

Acknowledgement—We are grateful for the useful comments given by Marc van der Burg on an early version of the manuscript.

REFERENCES

1. A. C. F. Cocks and M. F. Ashby, *Prog. Mater. Sci.* **27,** 189 (1982).
2. A. S. Argon, *Recent Advances in Creep and Fracture of Engineering Materials and Structures* (edited by B. Wilshire and D. R. J. Owen), pp. 1–52. Pineridge Press, Swansea (1982).
3. B. F. Dyson, *Metal Sci.* **10,** 349 (1976).
4. J. R. Rice, *Acta metall.* **29,** 675 (1981).
5. V. Tvergaard, *J. Mech. Phys. Solids* **32,** 373 (1984).
6. V. Tvergaard, *J. Mech. Phys. Solids* **33,** 447 (1985).
7. E. Van der Giessen and V. Tvergaard, *Int. J. Fracture* **48,** 153 (1991).
8. K. J. Hsia, D. M. Parks and A. S. Argon, *Mech. Mater.* **11,** 43 (1991).
9. E. Van der Giessen and V. Tvergaard, *Acta metall. mater.* **42,** 959 (1994).
10. E. Van der Giessen and V. Tvergaard, *Modelling Simul. Mater. Sci. Engng* **2,** 721 (1994).
11. S. Baik and R. Raj, *Metall. Trans. A* **13A,** 1215 (1982).
12. A. Pineau, *Advances in Fatigue Science and Technology* (edited by C. Moura Branco and L. Guerra Rosa), pp. 283–311. Kluwer Academic Publ., Dordrecht (1989).
13. H. Riedel, *Fracture at High Temperatures*. Springer Verlag, Berlin (1987).
14. E. Van der Giessen and V. Tvergaard, *Mech. Mater.* **17,** 47 (1994).
15. M. F. Ashby, *Surface Sci.* **31,** 498 (1972).
16. F. Ghahremani, *Int. J. Solids Struct.* **16,** 847 (1980).
17. B. Budiansky, J. W. Hutchinson and S. Slutsky, *Mechanics of Solids* (edited by H. G. Hopkins and M. J. Sewell), pp. 13–45. Pergamon Press, Oxford (1982).
18. A. Needleman and J. R. Rice, *Acta metall.* **28,** 1315 (1980).
19. T.-L. Sham and A. Needleman, *Acta metall.* **31,** 919 (1983).
20. J. W. Hutchinson, *Acta metall.* **31,** 1079 (1983).
21. H. S. Nielsen and V. Tvergaard, Intergranular fracture under creep-fatigue interaction, DCAMM Report No. 505; *Int. J. Damage Mech.* (to appear) (1995).